Elastic behavior of confined soap froth

Pierre Guyot, Andrew M Kraynik, Douglas Reinelt, Sylvie Cohen-Addad

Journal Name

ARTICLE TYPE

Cite this: DOI: 00.0000/xxxxxxxxxx

Elastic behavior of confined soap froth

Pierre Guyot,[a] Andrew M. Kraynik,[b] Douglas Reinelt[c] and Sylvie Cohen-Addad*[ad]

Received Date
Accepted Date

DOI: 00.0000/xxxxxxxxxx

The elastic response of ordered 3D soap froth, in which N layers of cells are confined between two rigid walls, is analyzed. Surface Evolver simulations are used to compute the equilibrium structure, which consists of a layer of Fejes-Toth cells at each wall and $N-2$ core layers of Kelvin cells. The reference state corresponds to the plate spacing h_o that achieves isotropic stress; and the foam confinement is varied by changing h. The foam is sheared in two orthogonal directions to determine elastic behavior up to the elastic limit or yield strain, which corresponds to the onset of topological transitions. The shear moduli in both directions decrease as N increases and slowly converge to the values of bulk Kelvin foam; the dependence on N is well described by a three-layer model consisting of Fejes-Toth cells and a core of Kelvin cells that deform like bulk foam. The influence of foam confinement on the elastic limit is studied. The topological transitions are compared to those in bulk Kelvin foam.

1 Introduction

Aqueous foams are dense packings of gas bubbles in a surfactant solution[1,2]. Despite being solely constituted of fluids, they exhibit remarkable elastic properties arising from the surface energy stored in the liquid-gas interfaces under mechanical loading. Under small strain, they behave as a linear elastic solid. Large strains and the corresponding large bubble distortions result in unstable configurations that violate equilibrium and provoke topological transitions. During these transitions bubbles lose contact and separate from neighbors; this is the fundamental mechanism for yielding and is essential for flow.

Due to their rheological properties, aqueous foams are sought for in a variety of applications[3]. Foams have been extensively used at large scale as displacing fluids in geological reservoirs in EOR processes[4], as fracturing fluid in drilling operations[3], or as chemical contaminant carriers for aquifer remediation[5]. Foam flow in porous media is mimicked in laboratory by model porous microfluidic systems[6–9]. Flow in confined geometries is used to manipulate bubbles in foams or droplets in concentrated emulsions for the purpose of building miniaturized labs on a chip[10–14]. In these processes where foam deformation is influenced by the confined geometry, their structure must accommodate the shape of a narrow channel or a pore of characteristic size of the order of a few bubble diameters. This raises the question how confinement impinges on the foam rheological behavior.

The rheological properties of 3D bulk foams have been extensively studied experimentally, numerically and theoretically[15,16]. Besides surface tension and bubble size, their static elastic properties such as shear modulus or yield stress depend on the volume fraction of the liquid phase and on the structural order. Rheology of foams under extreme confinement in pores of size equal to that of a single soap film has been investigated by numerical and experimental studies[17]. The impact of confinement specifically on the elastic behavior of a 3D foam has not yet been studied. Here, we consider ideal confined foams in the sense that: i) their liquid content is vanishingly small (soap froth or so-called dry foams); ii) they involve monodisperse ordered packings ; iii) they are confined between two parallel rigid plates separated by a gap distance of the order of a few bubble diameters.

In this paper, we study numerically the elastic behavior of dry confined multilayer foams in response to an applied shear. We address the following questions: How different is the shear modulus of a confined foam compared to that of a bulk 3D foam? What is the impact of the confinement, i.e. the plate spacing, on the shear modulus and how does it depend on the number N of bubble layers? Then we turn to large deformations and ask how the shear induced topological transitions, known as T1s, and their onset compare to those in a bulk foam. Using the Surface Evolver, we determine the shear moduli in the linear elastic regime and the stress-strain relationship up to the onset of T1s. We study the effect of confinement on yield stress and yield strain as a function of the layer structure.

[a] *Sorbonne Université, CNRS-UMR7588, Institut des NanoSciences de Paris, 4 place Jussieu, 75005 Paris, France.*
[b] *Sandia National Laboratories (Retired), Albuquerque, New Mexico, USA.*
[c] *Department of Mathematics, Southern Methodist University, Dallas, Texas 75275-0156 USA.*
[d] *Université Paris-Est Marne-la-Vallée, 5 Bd Descartes, Champs-sur-Marne, 77454 Marne-la-Vallée cedex 2, France.*
* *E-mail: sylvie.cohen-addad@insp.upmc.fr*

2 Multilayer dry foam structure

2.1 Soap froth multilayer between two rigid walls

The equilibrium structure of an ideal bulk 3D foam (soap froth) satisfies Plateau's laws[1], where each thin film separating adjacent bubbles has uniform curvature, the films meet 3 by 3 at equal angles of 120°, and the edges at the junctions between films, the so-called Plateau borders, meet 4 by 4 at vertices located at the center of regular tetrahedra. The Kelvin foam is the quintessential perfectly ordered monodisperse soap froth and is encountered in many real situations[2,18–20]. However, it cannot accommodate the geometrical constraint of a rigid wall. At mechanical equilibrium with a rigid plane wall, the films that do not lie along the wall must form 90° angles with the wall. As first pointed out by Fejes-Toth[21] and later by Weaire[2], this surface accommodation can be accomplished by a layer of Fejes-Toth (FT) cells. In this study, we consider a thin slab of a multilayer dry 3D foam confined between two parallel rigid plates. The foam consists of N = 2, 3, ... , 11 ordered layers of monodisperse bubbles with FT cells at each wall and N - 2 core layers of Kelvin cells in between, as illustrated in Fig. 1.

2.2 Kelvin structure

Let us recall the structure and the elastic properties of a Kelvin foam[1]. The Kelvin cell is a tetrakaidecahedron with 6 flat quadrilateral faces and 8 curved regular hexagonal faces (with zero mean curvature), as shown in fig. 2a. All the edges have the same length. Its equilibrium structure can be determined by minimizing surface energy density using the Surface Evolver, a standard software for discrete surface energy minimizations[23]. The cell exhibits cubic symmetry, the symmetry axes (x_o, y_o, z_o) pointing from the bubble center to the center of each square face. The Kelvin foam is a dense packing of Kelvin cells of identical volume, shape and orientation, where the bubble centers occupy the sites of a body-centered cubic lattice (bcc).

The linear elastic behavior of a Kelvin foam has been extensively studied[22]. The stress $\boldsymbol{\sigma_0}$ and strain $\boldsymbol{\varepsilon_0}$ tensors of a structure with cubic symmetry can be expressed relative to the crystallographic axes (x_o, y_o, z_o) using three independent elastic constants c_{11}, c_{12} and c_{44} (cf. definition in the appendix 7). We define the two independent shear moduli:

$$\begin{array}{rcl} G_1 & = & c_{44} \\ G_2 & = & \frac{1}{2}(c_{11} - c_{12}) \end{array} \qquad (1)$$

Kraynik and Reinelt showed that for the Kelvin foam, $G_1 = 0.96456$ and $G_2 = 0.57064$ in units of $T/V^{1/3}$, where T is the liquid-gas interfacial tension and V is the bubble volume[22].

2.3 Fejes-Toth structure

The Fejes-Toth cell is obtained by cutting in two halves a Kelvin cell so that the resulting polyhedron has a flat hexagonal base, and by slightly extending it to keep its volume equal to that of the original Kelvin cell. Two layers of Fejes-Toth (FT) cells can completely fill the space between two parallel walls. Such a FT bilayer resembles that of the bee honeycomb structure[21].

Figures 2a to c illustrate the scheme followed to build a FT cell. It is obtained by rotating the Kelvin cell 45° about one crystallographic axis (x_o-axis for instance in fig. 2a), cutting the cell in two halves along the mid-plane (x-y) perpendicular to the square face, and then stretching it in the z direction such that the new cell has the same volume V as the initial Kelvin cell. The x, y, z axes define the reference frame in the following. The resulting Fejes-Toth cell has tetragonal symmetry, with 11 faces: a (non regular) hexagon in the x-y plane, 2 regular hexagons, 2 quadrilateral faces, 4 irregular pentagons and 2 rectangular faces as illustrated in fig. 2c-f). Its equilibrium structure is determined by minimizing surface energy density using the Surface Evolver. This mechanical relaxation produces curved faces required to satisfy Plateaus' laws.

The equilibrium boundary condition at the wall is matched by placing the FT cell with its hexagonal base parallel to the x-y plane so that the films that do not lie along the wall form 90° angles with the wall. A set of two FT cells packed upside down along the z direction, in the same orientation, allows space filling without overlapping or voids when it is translated in the x and y directions as illustrated in fig. 1a. Similarly a set of two external FT cells with a core of $N-2$ Kelvin cells in the same orientation fill space when translated along the x-y plane as shown for $N = 3$ in fig. 1b.

3 Computation of multilayer structure and stress response

3.1 Stress derivation

We consider an ordered multilayer foam, confined between two plates perpendicular to the z direction, separated by a gap distance h, and infinitely extended in the (x-y) plane (cf. fig. 1). The structure is described by the three lattice vectors $\mathbf{p_1}$, $\mathbf{p_2}$, $\mathbf{p_3}$ which set the unit cell:

$$\begin{array}{rcl} \mathbf{p_1} & = & (p_x, p_y, 0) \\ \mathbf{p_2} & = & (-p_x, p_y, 0) \\ \mathbf{p_3} & = & (0, 0, h) \end{array} \qquad (2)$$

The vectors $\mathbf{p_1}$ and $\mathbf{p_2}$ join the centers of two neighboring (hexagonal) faces at the lower plate. Their length is expressed in units of $V^{1/3}$. An homogeneous deformation, defined by the deformation gradient tensor $\mathbf{F}$, is applied to the foam slab, by displacing the initial lattice vectors to get the new lattice vectors $\mathbf{p_i'}$ such that :

$$\mathbf{p_i'} = \mathbf{F} \cdot \mathbf{p_i} \qquad (3)$$

The average macroscopic stress of the foam multilayer is then evaluated using Batchelor's general expression of the stress induced by a quasistatic strain in a fluid consisting of two immiscible phases[24]. Omitting the isotropic term due to the gas pressure in each bubble, the contribution of the interfacial tension forces exerted on each individual film is given by[25]:

$$\sigma_{ij} = \frac{T}{V_f} \int_{S_{int}} (\delta_{ij} - n_i n_j)\, \mathrm{d}s \qquad (4)$$

where S_{int} is the area of all liquid-gas interfaces in the volume of foam V_f, δ_{ij} is the Kronecker delta, n_i is a local unit vector normal to the interface, and ds is the differential area element. Since the considered foam structures are periodic, the integral Eq. 4 needs

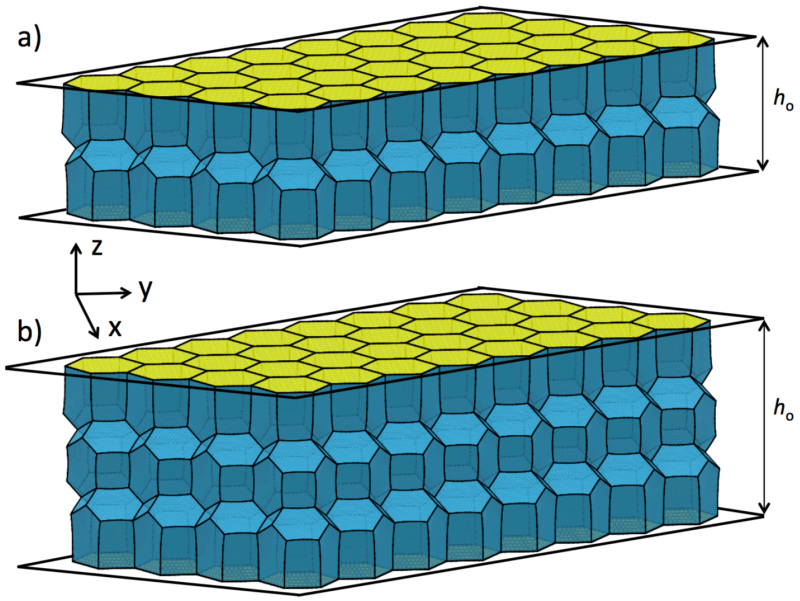

Fig. 1 Structure of multilayer foams confined between two parallel walls (represented by the rectangular frames) normal to the z direction. The cell faces in contact with the wall are shown in yellow. a) A bilayer ($N = 2$) consisting of 2 Fejes-Toth cell layers; b) A trilayer ($N = 3$) consisting of two Fejes-Toth cell layer in contact with each wall and a core layer of Kelvin cells. The multilayers have relaxed isotropic structure with lattice parameters given in table 1 (See text for definition.) corresponding to gap separation h_o.

only to be evaluated over the unit cell. In the following, we will consider the situation where each plate surface is wetted by a thin liquid film, assuming total wetting of the wall by the liquid phase. This case is indeed frequently encountered in experimental or practical situations. As a consequence, Eq. 4 can be written as:

$$\sigma_{ij} = \frac{T}{V_c}\left(2\left(\sum_{\substack{k=1\\ k\notin wall}}^{F}\int_{S_k}(\delta_{ij}-n_i n_j)\,\mathrm{d}s\right)+2\int_{S_w}(\delta_{ij}-n_i n_j)\,\mathrm{d}s\right) \tag{5}$$

Here V_c is the volume of the unit cell containing F films, S_k is the area of a film k shared by two bubbles in the unit cell. The factor of 2 in the first term of the r.h.s. of Eq. 5 accounts for the two liquid-gas interfaces of each film in the interior of the slab. S_w denotes the area of one hexagonal film wetting the wall, such a film having only one liquid-gas interface. By symmetry, the bottom wall film ($z = 0$) and the top film ($z = h$) have the same area. Thus the factor of 2 in the second term of the l.h.s. of Eq. 5 stands for the 2 wall films per unit cell.

3.2 Surface Evolver simulations

Applying affine deformations using the lattice transformation Eq. 3 generates foam structures that violate Plateau's laws. Equilibrium relaxed structures are then obtained using the Surface Evolver. The structure is initially discretized such that each n-sided face is subdivided into n flat (linear mode) triangular facets. This initial mesh can be refined, so that the Ri discretized structures has 4^i times many more facets than the initial R one. Additionally, the facet can be quadratically interpolated (quadratic mode) to gain accuracy at the cost of time calculation. In this study, the surface energy density is minimized with the constraint of fixed bubble volume. This minimization is performed by successive iteration steps using a conjugate gradient algorithm repeated until the convergence is reached. A given strain (shear or stretch) is applied to the structure by applying the deformation gradient tensor $\mathbf{F}$ to each lattice vector $\mathbf{p_i}$ of the unit cell. This defines the new lattice vectors and determines the new position of the vertices in the unit cell. Then the surface is recalculated and its energy minimized. At each minimization step, the stress is evaluated using Eq. 5. The criterion for convergence is based on the stress evaluation as in[22]. For a precision of n digits on the stress, we insure that the $n+1$ digit does not vary upon further steps. Lengths and stresses are expressed in $V^{1/3}$ and $T/V^{1/3}$ units respectively.

3.3 Determination of the relaxed lattice parameters

Since the FT structure has a tetragonal symmetry, the plate spacing h and the lattice vector parameters p_x, p_y must be independently adjusted to achieve isotropic stress. For a given number N of layers, the values of these three parameters are unique. They are determined, for each N value, using repeated tension-compression annealing cycles in the 3 space directions. For instance, uniaxial extension is applied in the z direction. Then the vertices and edges in contact with the wall are let free to move as the structure is relaxed using the Evolver (in quadratic $R2$ refinement mode). The extension is repeated with small strain increments until the stress difference $\sigma_{xx} - \sigma_{yy} = 0$ with 7 significant digits. A similar elastic recoil is performed in the x and y directions until $\sigma_{zz} - \sigma_{yy} = 0$ and $\sigma_{xx} - \sigma_{xx} = 0$. This procedure determines with 6 significant digits the relaxed lattice parameters,

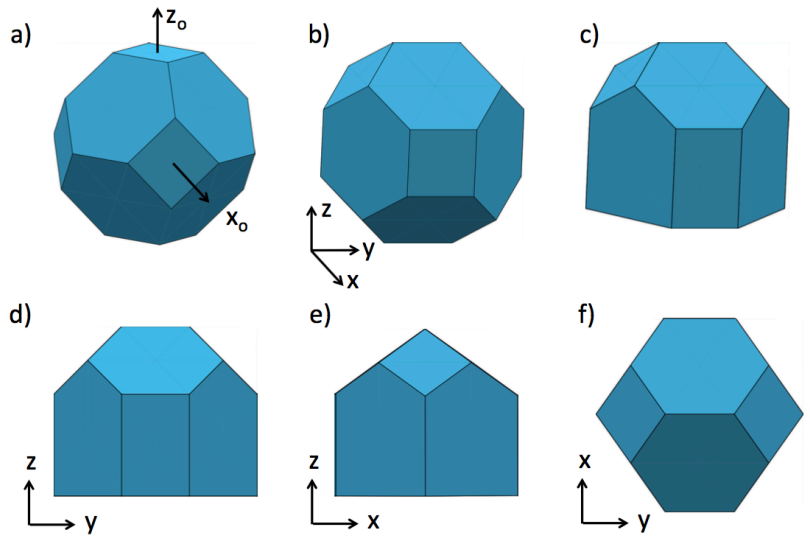

Fig. 2 Structure of Kelvin and Fejes-Toth (FT) bubbles in a dry multilayer. a) A Kelvin cell with its crystallographic axes x_o, y_o, z_o. b) A Kelvin cell rotated by $45°$ around the x_o axis. c) A FT cell obtained by cutting the Kelvin cell in b) along a plane perpendicular to the square face, and stretched along the z direction such that it has the same volume as the original Kelvin cell. The axes x, y, z refer to the fixed reference frame. d), e), f) give three orthogonal views of the FT cell. The FT structure matches the boundary condition of $90°$ angles between the films and the x-y plane.

denoted p_{xo}, p_{yo}, h_o, in the reference undeformed state for each N value, as listed in Table 1. Moreover, we deduce from the data for $N = 2$, the thickness of one relaxed FT layer: $\delta = h_o/2 = 0.97765$. Figure 3 shows that the total thickness of the relaxed N-multilayer foam varies linearly with N. In the following, the degree of confinement of a N-multilayer in a gap thickness h is characterized by the confinement ratio defined as:

$$r = h/h_o \tag{6}$$

Table 1 Lattice parameters (expressed in $V^{1/3}$ units) of the N-multilayers as defined in eq. 2. They are determined by requiring the stress of the "undeformed" foam to be isotropic. The boundary condition at the wall corresponds to total wetting by the liquid film

N	p_{xo}	p_{yo}	h_o
2	0.56398	0.90682	1.95530
3	0.58148	0.90398	2.85360
5	0.59805	0.90030	4.64310
7	0.60606	0.89823	6.42922
9	0.61085	0.89689	8.21354
11	0.61400	0.89596	9.99706

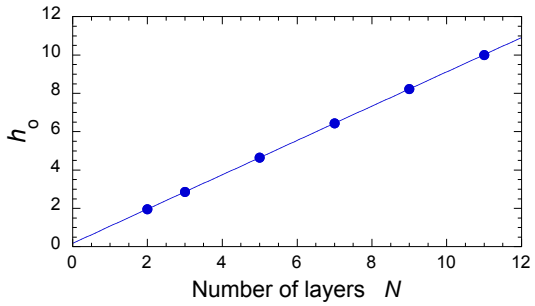

Fig. 3 Thickness of the relaxed isotropic N-multilayer as a function of the total number N of layers. The symbols correspond to the data of Table 1. The line is a linear regression to the data: $h_o = 1.9553 + (0.8940 \pm 0.0003)(N-2)$.

4 Linear elastic response

4.1 Shear modulus and normal stresses differences computation.

Since the multilayer structure is anisotropic, we study its elastic response as it is subjected to simple shear in the x-y plane, along either the x or the y direction (cf. Fig. 1). For a given confinement ratio r, we determine the reference relaxed state where the stress in the x-y plane is isotropic. By mechanical annealing with the contact line at the wall being free to move, we perform successive elastic recoils until $\sigma_{xx} - \sigma_{yy} = 0$. After this step, the stress tensor components σ_{xy}, σ_{yz} and σ_{xz} are equal to zero with 7 significant digits. Then we impose that the edges and vertices in contact with each wall are fixed and, we apply a simple shear as given by Eq. 3. This corresponds to the situation where the instantaneous elastic response is probed without foam slip at the wall. For a real foam, pinning at the wall is indeed achieved at the instant where the stress is applied, before any viscous relaxation process in the wetting liquid films occurs. The structure is further relaxed with R2 refinement (in quadratic mode) and the stress components are evaluated using Eq. 5. Stresses and shear moduli are scaled by $T/V^{1/3}$.

For simple shear in the x direction, the deformation gradient tensor $\mathbf{F}$ and the infinitesimal strain tensor ε are:

$$F_{ij} = \begin{pmatrix} 1 & 0 & \gamma \\ 0 & 1 & 0 \\ 0 & 0 & 1 \end{pmatrix} \qquad \varepsilon_{ij} = \begin{pmatrix} 0 & 0 & \gamma/2 \\ 0 & 0 & 0 \\ \gamma/2 & 0 & 0 \end{pmatrix} \tag{7}$$

We define the shear modulus G_{xz} in that direction by:

$$\sigma_{xz} = G_{xz}\gamma \tag{8}$$

and the shear induced normal stress differences:

$$\begin{array}{rcl} N_1 & = & \sigma_{xx} - \sigma_{zz} \\ N_2 & = & \sigma_{zz} - \sigma_{yy} \end{array} \tag{9}$$

We deduce G_{xz} from the variations of σ_{xz} with γ as the strain is increased by small increments in the range where the response is linear. We do similarly for simple shear in the y direction with

$$F_{ij} = \begin{pmatrix} 1 & 0 & 0 \\ 0 & 1 & \gamma \\ 0 & 0 & 1 \end{pmatrix} \qquad \varepsilon_{ij} = \begin{pmatrix} 0 & 0 & 0 \\ 0 & 0 & \gamma/2 \\ 0 & \gamma/2 & 0 \end{pmatrix} \tag{10}$$

and define the shear modulus G_{yz} as:

$$\sigma_{yz} = G_{yz}\,\gamma \tag{11}$$

and the shear induced normal stress differences:

$$\begin{array}{rcl} N_1 & = & \sigma_{yy} - \sigma_{zz} \\ N_2 & = & \sigma_{zz} - \sigma_{xx} \end{array} \tag{12}$$

In the next paragraphs, we study the impact of the confinement ratio r (eq. 6) on both moduli G_{xz} and G_{yz} for N-multilayer as N is varied between 2 and 11.

4.2 Bilayer shear modulus.

First we study the linear elastic response of a bilayer. Fig. 4 shows the structure of the periodic cell as the bilayer is squeezed ($r < 1$) or stretched ($r > 1$). We recall that $r = 1$ corresponds to the isotropic state (cf. eq. 6). In this range of r, there are no topological changes of structure. For the non confined bilayer ($r = 1$), we represent in figure 5 the variations of the shear stress and both normal stress differences as a function of the applied strain γ increased by steps of 0.002 up to 0.02. From the shear stress data, we deduce: $G_{xz,o} = 1.37010 \pm 2.10^{-5}$ and $G_{yz,o} = 0.77688 \pm 3.10^{-5}$. This shows that the elastic behavior is anisotropic. The bilayer is stiffer when sheared along the x direction compared to the y direction. The shear stress results from the traction that the films in contact with the wall and perpendicular to it exert on the contact lines. Since the surface tension acts in the plane tangential to the film at the contact line, a film contributes to the shear stress as long as it is not aligned with the shear direction. Thus for the x-z strain, all 6 films contribute whereas for the y-z strain, only 4 films contribute (cf. fig. 6). Neglecting the exact cell geometry, this simple argument suggests that G_{xz} should be about 1.5 times larger than G_{yz} which is indeed the case.

By fitting the normal stress difference data to a quadratic polynomial, we get for x-z shear: $N_1 = (1.797 \pm 0.001)\gamma^2$ and $-N_2 = (1.158 \pm 0.001)\gamma^2$, and for those induced by a y-z shear: $N_1 = (1.982 \pm 0.008)\gamma^2$ and $-N_2 = (1.053 \pm 0.001)\gamma^2$. We observe that the normal stresses induced by shear in the bilayer are anisotropic. For isotropic materials with shear modulus G, the general Poynting relationship holds[26]: $N_1 = \sigma_{12}\,\gamma$, which reduces to $N_1 = G\gamma^2$ for small γ. This relation is predicted to hold for Kelvin foams if the stress is averaged over all possible orientations[27]. For bilayers, the numerical simulations show that $N_1/(G\gamma)^2$ is 1.31 or 2.55, which confirms that the elastic behavior exhibits significant anisotropy.

Then we vary the degree of confinement with respect to the reference isotropic state. Figure 7a shows the variations of both shear moduli as a function of the confinement ratio $r = h/h_o$. We observe that the moduli strongly increase with r. When the bilayer is compressed from the reference state, the area S_w of the hexagonal basis on the wall increases, thus the number of films per unit surface pulling on the wall decreases. At the same time, the tension exerted on the films increases since the perimeter L of the base increases. The results show that the effect of the area dominates, leading to a global decrease of the modulus as the compression increases. We plot in Fig. 7b the variations of the moduli normalized by their value in the reference state ($r = 1$), denoted $G_{xz,o}$ and $G_{yz,o}$ respectively. The numerical results show that, to second order in r, the relative variations of the moduli normalized by their value in the reference state ($r = 1$), denoted $G_{xz,o}$ and $G_{yz,o}$ respectively, are well described by the polynomial functions:

$$\frac{G_{xz}}{G_{xz,o}} = 1 + 0.909(r-1) - 0.27(r-1)^2 \tag{13}$$

$$\frac{G_{yz}}{G_{yz,o}} = 1 + 1.107(r-1) - 0.11(r-1)^2 \tag{14}$$

4.3 Trilayer shear modulus.

We simulate the shear elastic linear response of a trilayer similarly to that of a bilayer. We deduce its shear moduli G_{xz} and G_{yz} from the variations of the stress response to applied strain up to 0.02. In the isotropic state ($r = 1$), we find : $G_{xz,oT} = 1.22500 \pm 2.10^{-5}$ and $G_{yz,oT} = 0.67537 \pm 2.10^{-5}$. The results in fig. 7a show the variations of G_{xz} and G_{yz} with the confinement ratio r. The large difference observed between G_{xz} and G_{yz} reflects the anisotropy of the trilayer structure. On both shear directions the trilayer foam becomes stiffer as the ratio r increases. The numerical results show that at second order in r, the variations of the moduli normalized by their value in the reference state are well described by the polynomial functions:

$$\frac{G_{xz}}{G_{xz,oT}} = 1 + 1.008(r-1) - 0.25(r-1)^2 \tag{15}$$

$$\frac{G_{yz}}{G_{yz,oT}} = 1 + 0.99(r-1) + 0.34(r-1)^2 \tag{16}$$

In the relaxed isotropic reference state ($r = 1$), our simulations show that the FT cell has an interfacial energy density, scaled by $T/V^{1/3}$, equal to $E_{o,FT} = 5.525$. This value is larger than that of an undeformed Kelvin cell[22]: $E_{o,K} = 5.306$. The larger value of $E_{o,FT}$ compared to $E_{o,K}$ reflects the supplementary cost of energy caused by the confining wall. The Kelvin cell in the core of the trilayer lowers the relative contribution of the FT cells to the total interfacial energy. Thus we expect the moduli of a trilayer to be lower than that of a bilayer, which is indeed the case. In the next section, we study the impact of the number of layers on the shear

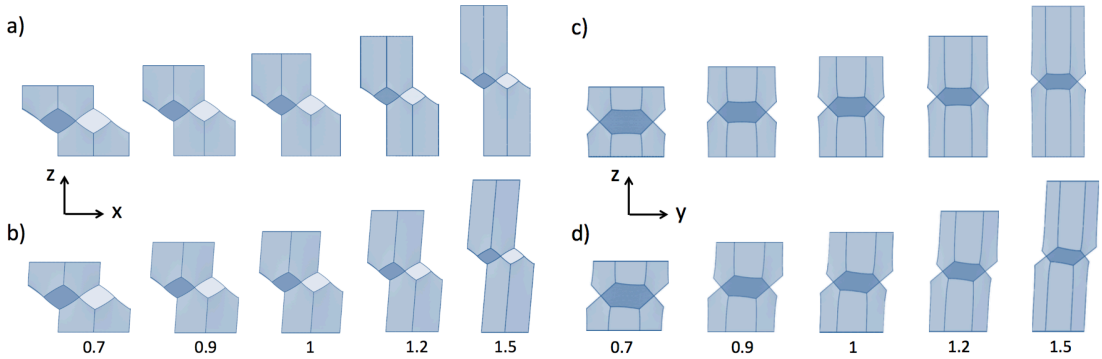

Fig. 4 Visualization of the relaxed periodic cell of a bilayer for different confining ratios $r = h/h_o$, varied between 0.7 and 1.5 as indicated, viewed along an orthogonal projection: a, b) on the x-z plane ; c, d) on the y-z plane. The cell is confined between two plates (not represented) normal to the z direction separated by a distance h. The value $r = 1$ corresponds to the isotropic reference state. See section 3.1. a) and c) show the undeformed bilayers. b) (resp. d) show the relaxed structure as the bilayer is sheared in the x (resp. y) direction. A large strain $\gamma = 0.1$ is applied for the visualization, but much smaller strains are used to calculate the shear moduli.

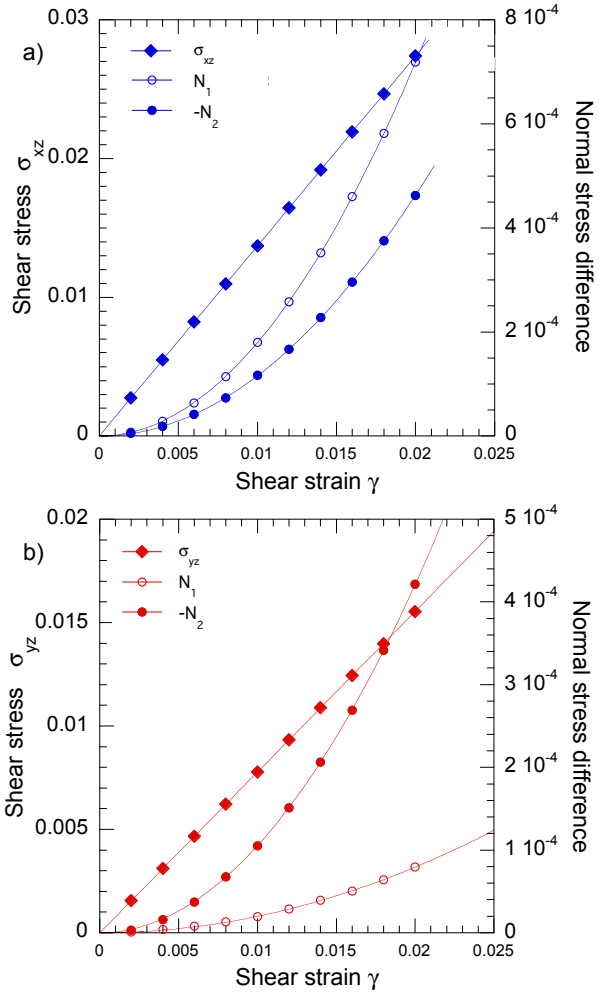

Fig. 5 Variations of the shear stress (♦), the first (○) and second (•) normal stress differences of a bilayer subjected to a shear strain γ : a) in the x direction, b) in the y direction. The lines represent a linear fit for the shear stress and quadratic fits for N_1 and N_2 (see text). The stresses are expressed in $T/V^{1/3}$ units.

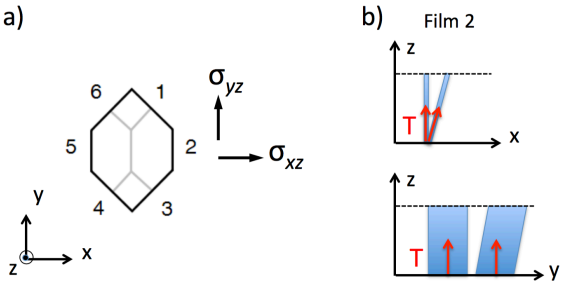

Fig. 6 a) Orthogonal projection of the undeformed FT bilayer showing the hexagonal basis in contact with the wall. Under a x-z shear, all 6 perpendicular films contribute to the shear stress σ_{xz}. Under a y-z shear, films labeled 2 and 5 remain parallel to the direction of motion. Thus the surface tension remains perpendicular to the plate and does not contribute to the shear stress σ_{yz}. b) Schematic drawing of surface tension acting on film 2 undergoing a x-z strain (top) or a y-z strain (down).

moduli.

4.4 N-layer shear modulus.

In this section, we consider multilayers in their isotropic undeformed reference state corresponding to a confinement ratio $r = 1$ (cf. Fig. 8) and, we analyze their response to an applied shear strain in the linear domain. As for the previous bi- and trilayers, we apply increasing shear strains ranging between 0.002 to 0.02, in either x or y directions and we deduce the corresponding shear moduli G_{xz} and G_{yz} from linear fits to the stress-strain data.

In Figure 10, we plot both shear moduli as a function of the number of layers N. As N increases from 2 to 11, we see that G_{xz} and G_{yz} both decrease monotonously. To evaluate the impact of confinement on the multilayer stiffness, we compare their shear moduli to those of a bulk Kelvin foam, evaluated in directions that correspond to similar orientations in the multilayer and in the Kelvin foam. For instance, let us consider a shear deformation ε_{xz} applied to the N-multilayer along direction x (as defined in Fig. 1 or 2d-f). In a Kelvin foam, such a deformation would be equivalent to that obtained after rotating the cell crystallographic

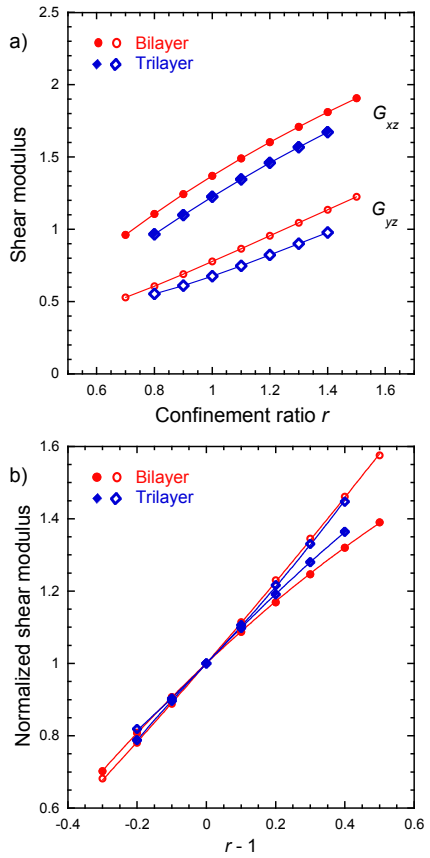

Fig. 7 Bilayer ($N = 2$) and trilayer ($N = 3$) shear moduli. a) Variation of G_{xz} and G_{yz} as a function of the confinement ratio $r = h/h_o$ when the foam is sheared in either x (filled symbols) or y (empty symbols) direction. The moduli are scaled by $T/V^{1/3}$. b) Moduli normalized by their value for $r = 1$ plotted as a function of $r - 1$. The continuous lines are quadratic fits to the data (Eq. 13 and 14). Same symbols as in a).

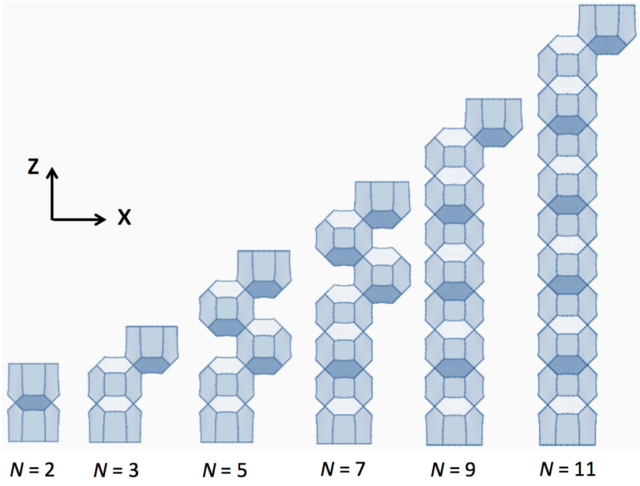

Fig. 8 Basic cell of the N-multilayer foam structure. It consists of one Fejes-Toth cell at the bottom, one at the top, and $N - 2$ Kelvin internal cells. The basic cell is infinitely repeated in the x and y directions. The parallel confining plates (not shown) lie in the x-y planes. The represented structures correspond to the lattice parameter h_o (or $r = 1$) in the z direction such that the multilayer is in its reference isotropic state.

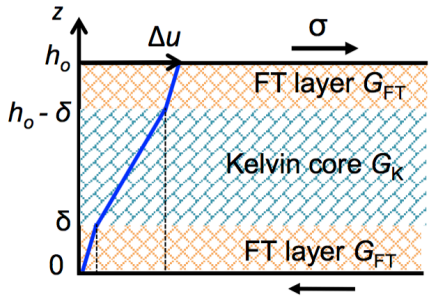

Fig. 9 Schema of the multilayer foam consisting of 3 independent layers. An applied shear stress σ induces local displacements in each layer that add up to build the total displacement Δu.

axis 45° about the x_o axis (cf. Fig. 2a), and then shearing the cell along the x direction. The calculation given in the appendix 7 shows that:

$$\sigma_{xz} = G_1 \gamma \tag{17}$$

where G_1 is defined by Eq. 1. Thus the multilayer shear modulus G_{xz} can be compared to the shear modulus G_1 of a bulk Kelvin foam. Similarly a simple shear deformation ε_{yz} applied to a Kelvin cell in the reference frame of Fig. 2d-f is equivalent to that obtained after rotating the cell crystallographic axis 45° about the x_o axis (cf. Fig. 2a), and then shearing the cell along the y direction. The calculation given in the appendix 7 shows that:

$$\sigma_{yz} = G_2 \, \gamma \tag{18}$$

with $\gamma = 2\varepsilon_{yz}$. Hence the multilayer shear modulus G_{yz} can be compared to the shear modulus G_2 of a bulk Kelvin foam. The data in Fig. 10 show that the shear moduli indeed asymptotically converge toward both values G_1 and G_2 expected for a bulk Kelvin foam.

To model the multilayer elasticity, we consider the structure to consist of three *independent* stacked layers (cf. Fig. 9): A core layer made of a Kelvin foam, with shear modulus G_K, sandwiched between two FT surface layers with modulus G_{FT} . A uniform shear stress σ applied to such a composite structure induces a local strain in the core layer:

$$\gamma_K = \sigma / G_K \, , \tag{19}$$

and in each FT layer:

$$\gamma_{FT} = \sigma / G_{FT} \, . \tag{20}$$

The local displacements in each layer add to build up the total displacement:

$$\Delta u = 2\delta \gamma_{FT} + (h_o - 2\delta)\gamma_K, \tag{21}$$

where h_o is the total thickness of the foam and δ is the thickness of one FT layer. We define the average strain:

$$\gamma_{av} \equiv \frac{\Delta u}{h_o} \, , \tag{22}$$

and the effective shear modulus of the composite layer:

$$G_{eff} \equiv \frac{\sigma}{\gamma_{av}} \,. \tag{23}$$

Combining Eq. 19 to 23 yields the expression:

$$\frac{h_o}{G_{eff}} = \frac{h_o - 2\delta}{G_K} + \frac{2\delta}{G_{FT}} \,. \tag{24}$$

As shown by the data of Table 1 and by Fig. 3, the total thickness varies linearly with N according to: $h_o = 2\delta + p(N-2)$ with $\delta = 0.97765$ and $p = \mathrm{d}h_o/\mathrm{d}N = 0.8940$. Thus the variations of the effective modulus with the number of layers can be written as:

$$G_{eff} = \frac{2\delta + p(N-2)}{\frac{2\delta}{G_{FT}} + \frac{p(N-2)}{G_K}} \tag{25}$$

We expect this relation to hold for both shear directions with the corresponding FT moduli $G_{xz,o}$ and $G_{yz,o}$ found for the the bilayer (cf. section 4.2) and with the Kelvin moduli G_1 and G_2 (cf. section 2). As can be seen in Fig. 10, this prediction captures remarkably well the softening of the multilayer foam, for both shear moduli, without any free parameter. The small difference between the data and the prediction can be attributed to the fact that the 3 layers are not completely independent and are not strictly separated at the distance δ from each plate. δ is the distance between a plate and the top of the pentagonal faces of the FT cells. A part from it, there is a thin zone where the FT cells and the Kelvin cells overlap. The local non-affine distortion of the structure in the overlapping zone is not taken into account in our model. Furthermore, we deduce from these results the minimum number of bubble layers an ordered dry foam must have for its shear moduli to be representative of those of a bulk foam sample. We see that the relative difference between G_{xz} and G_1 is less than 5% for $N \geq 14$ and that the relative difference between G_{yz} and G_2 is less than 5% for $N \geq 12$. This is important for practical applications where mechanical properties of a foam confined in channels or pores must be assessed. As an extension of this study, it would be interesting to determine the Young modulus of a N-multilayer in response to a uniaxial stretching or compression along the z-direction.

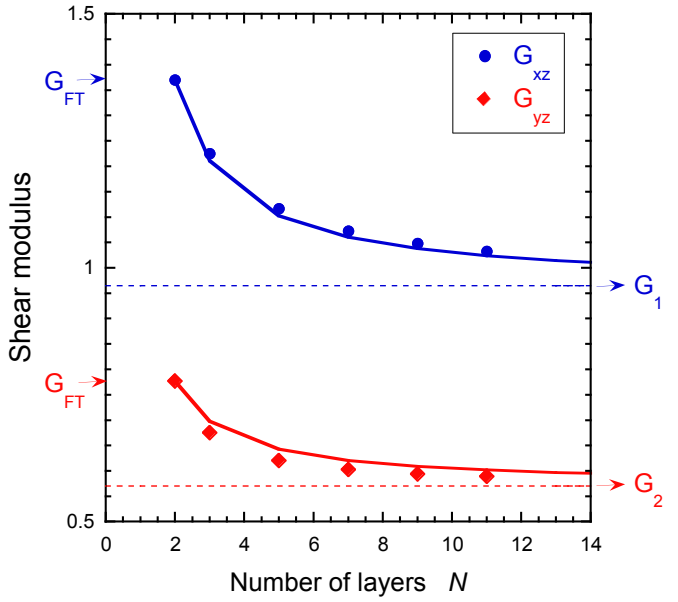

Fig. 10 Variation of the shear modulus of the multilayer foam as a function of the number of layers N. The symbols correspond to the data as labeled. The equivalent shear moduli for a bulk Kelvin foam are indicated as G_1 and G_2 (dotted lines, see text). The continuous full lines represent the prediction by the layer model (eq. 25) with the bilayer and Kelvin moduli: $G_{FT} = G_{xz,o} = 1.370$ and $G_K = G_1 = 0.965$ for the x-z shear and, $G_{FT} = G_{yz,o} = 0.777$ and $G_K = G_2 = 0.571$ for the y-z shear. The moduli are scaled by $T/V^{1/3}$.

5 Large deformations

5.1 Topological transitions.

As in section 4.1, we apply quasistatic deformations to multilayer foams with confinement in the range $0.7 < r < 1.5$ and increase strain by increments of 0.02. Using the Surface Evolver, the structure is relaxed with R2 refinement(quadratic mode) after each strain step, and the stress is evaluated using eq. (5). We observe the evolution of the structure as faces and edges deform up to the strain where Plateau's laws are violated, which provokes irreversible topological transitions.

Let us recall the topological transitions that occur in a Kelvin foam under shear; these T1s cause cells to switch neighbors but they remain Kelvin. Three types of transitions can be triggered[28]. 1) A standard T1 occurs when opposite edges of a shrinking quadrilateral face go to zero length. This leads to a pair of 5-fold vertices that violate Plateau's laws and is analogous to the T1 in 2D soap froth[29]. 2) A point T1 occurs when a quadrilateral face shrinks to a point. 3) A triple T1 happens when opposite long curved edges of a shrinking hexagonal face touch at their center. Figure 11 shows the evolution of a bilayer and a trilayer, initially in the isotropic reference state ($r = 1$) as they are sheared in the x direction. The areas of a quadrilateral face and a hexagonal face diminish as the strain γ increases. Two opposite long edges of the hexagonal face eventually touch, which produces an unstable junction and triggers a triple T1. This transition is consistent with triple T1 induced in bulk Kelvin foam. We recall that the shear stress σ_{xz} corresponds to the orientation 1.2 defined in ref.[28]. Triple T1s occur for all confinements: $0.7 < r < 1.5$ for bilayers and $0.8 < r < 1.4$ for trilayers.

Figure 12 shows the evolution of a bilayer and a trilayer, sheared in the y direction. As the strain γ increases, a square face shrinks to a point, triggering a point T1. Again, this transition is consistent with point T1 induced in bulk Kelvin foam since the shear stress σ_{yz} corresponds to the orientation 1.3 in ref.[28]. Point T1s occur for all investigated confinements.

5.2 Yield stress and yield strain of multilayer foams.

Figure 13 shows the variations of the shear stress with the strain, applied either in the x or y direction, for bilayers and trilayers with different confinements. The largest strain γ_y for each curve corresponds to the onset of topological transitions, the elastic limit, and the yield stress σ_y. Note that the shear stress σ_{yz} for the bilayers has a local maximum; consequently the yield stress associated

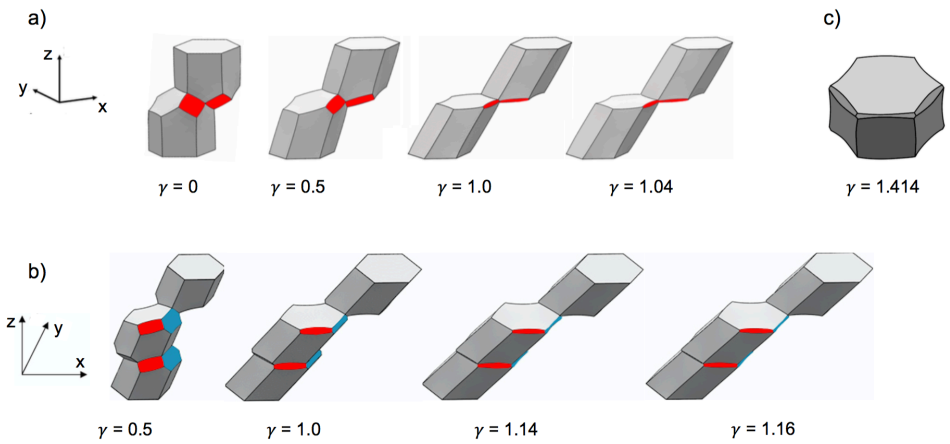

Fig. 11 Large shear deformations applied in the x direction, for different strain amplitudes $\gamma = 2\varepsilon_{xz}$ as indicated to: a) a bilayer with $r = 1$; b) a trilayer with $r = 1$. The area of the square (in red) and hexagonal (in blue) faces decrease. The two opposite long edges of the hexagonal faces will touch and trigger a triple T1, as in bulk Kelvin foam; c) a Kelvin cell sheared in the same orientation[28]. A triple T1 is triggered at the strain: a) $\gamma_y = 1.04$, b) $\gamma_y = 1.16$, c) $\gamma_{y,K} = 1.47$.

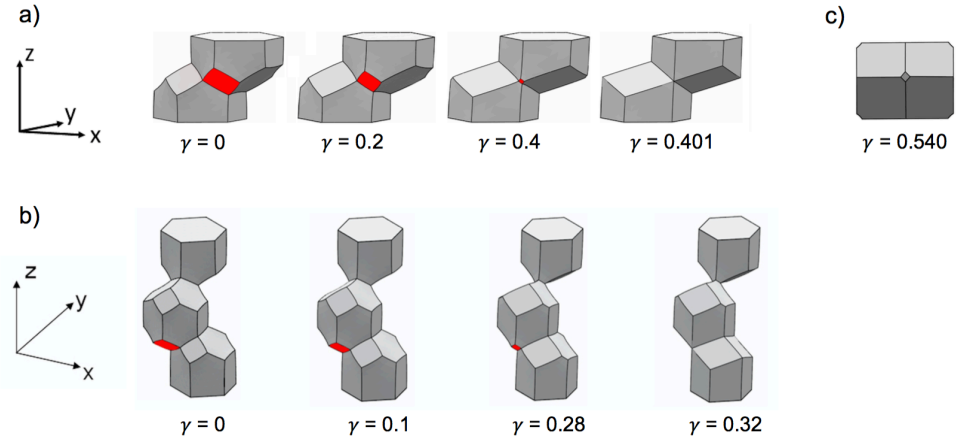

Fig. 12 Large shear deformations applied in the y direction, for different strain amplitudes $\gamma = 2\varepsilon_{yz}$ as indicated to: a) a bilayer with $r = 0.7$; b) a trilayer with $r = 1$. The square face (in red) contracts to a point and triggers a point T1, as in bulk Kelvin foam; c) a Kelvin cell sheared in the same orientation[28]. A point T1 is triggered at the strain a) $\gamma = 0.40$, b) $\gamma = 0.32$, c) $\gamma_{y,K} = 0.548$.

with the yield strain is lower than the maximum stress. This is an artifact of the ordered structure. For both shear directions, these variations are consistent with those observed in a Kelvin foam[28].

Finally, we show in figure 14, the variations of the yield strain of the multilayers as a function of r. Again, the mechanical response is anisotropic. γ_y is larger in the x-z direction than in the y-z direction. Moreover we observe that the yield strain, thus the onset of T1s, appears earlier since the multilayer foam is stretched. Upon stretching in the z direction, i.e. for increasing ratio r, the lateral faces become narrow. Thus they vanish for a smaller applied strain. As a consequence, the yield strain γ_y decreases as r increases.

Now we turn to the effect of the number of layers N. In the reference state with $r = 1$ where the multilayer can be compared to a bulk Kelvin foam, we see that the multilayer yields for smaller strains than the Kelvin foam. For the bilayer, where the foam is more restricted, γ_y is decreased by a factor of 0.7 and 0.4 in the x-z and y-z directions respectively. Figures 13 and 14 clearly show that the non-linear elastic response of ordered confined foams is highly orientation dependent. This anisotropic elastic behavior is also a characteristic of the Kelvin foam.

6 Summary

We have shown that the elastic response of ordered soap froth confined between two rigid walls is stiffer than bulk foam. The Surface Evolver was used to calculate the equilibrium structure and nonlinear elastic behavior of N layers of confined cells. The increased stiffness is well described by a simple micro-mechanical model with no free parameter, by assuming that the foam consists of three independent layers: a layer of Fejes-Toth cells at each wall and a core of Kelvin cells that deform like a bulk foam. The nonlinear elastic response was analyzed up to the elastic limit, which coincides with the onset of topological transitions and determines the yield stress and yield strain. This response is highly anisotropic, similar to the Kelvin foam; the shape of the stress-strain curve, yield stress and yield strain are all highly dependent on foam orientation. The point and triple topological transitions that occur in the present study are a consequence of the highly symmetric deformations considered. The standard T1 was not found, but is by far the most prevalent during shearing flow of a Kelvin foam. Predicting the elastic behavior of confined soap froth is relevant to foam rheology in porous media and in the narrow channel geometries encountered in miniaturized lab-on-a-chip applications for instance. Further developments should address the determination of the tensorial constitutive law in the domain of large strains, and the investigation of the elastic behavior of wet confined foams.

7 Appendix

For a crystal with cubic symmetry, the stress and strain tensor components expressed in the coordinate axes corresponding to the crystallographic axes $(x_o y_o z_o)$ (cf. fig. 2a) write[22,30]:

$$\begin{aligned}
\sigma_{xx} &= c_{11}\varepsilon_{xx} + c_{12}(\varepsilon_{yy} + \varepsilon_{zz}),\\
\sigma_{yy} &= c_{11}\varepsilon_{yy} + c_{12}(\varepsilon_{xx} + \varepsilon_{zz}),\\
\sigma_{zz} &= c_{11}\varepsilon_{zz} + c_{12}(\varepsilon_{xx} + \varepsilon_{yy}),\\
\sigma_{xy} &= 2c_{44}\varepsilon_{xy},\\
\sigma_{yz} &= 2c_{44}\varepsilon_{yz},\\
\sigma_{xz} &= 2c_{44}\varepsilon_{xz},
\end{aligned} \tag{26}$$

In the reference frame (xyz) (cf. fig 2d,e,f), a shear strain γ applied along the x direction in the plane normal to the z direction is described by the strain tensor:

$$\varepsilon_{ij} = \begin{pmatrix} 0 & 0 & \gamma/2 \\ 0 & 0 & 0 \\ \gamma/2 & 0 & 0 \end{pmatrix} \tag{27}$$

The corresponding strain tensor $\boldsymbol{\varepsilon_o}$ in the crystallographic frame $(x_o y_o z_o)$ is such that:

$$\boldsymbol{\varepsilon_o} = Q_x \, \boldsymbol{\varepsilon} \, Q_x^{-1}, \tag{28}$$

where Q_x is the rotation matrix that performs counterclockwise rotation of 45 deg around the x axis. The stress tensor σ_o in the crystallographic frame is then given by Eq. 26. Finally the stress tensor σ in the reference frame is deduced from:

$$\sigma = Q_x^{-1} \, \sigma_o \, Q_x \,, \tag{29}$$

which reads:

$$\begin{aligned}
\sigma_{xx} &= \sigma_{yy} = \sigma_{zz} = 0\,,\\
\sigma_{xy} &= \sigma_{yz} = 0\,,\\
\sigma_{xz} &= c_{44}\,\gamma\,,
\end{aligned} \tag{30}$$

Similarly, a shear strain γ applied along the y direction in the plane normal to the z direction is described by the strain tensor:

$$\varepsilon_{ij} = \begin{pmatrix} 0 & 0 & 0 \\ 0 & 0 & \gamma/2 \\ 0 & \gamma/2 & 0 \end{pmatrix} \tag{31}$$

Calculating the strain and stress tensors in the crystallographic frame using eq. 28 and 29 gives:

$$\begin{aligned}
\sigma_{xx} &= \sigma_{yy} = \sigma_{zz} = 0\,,\\
\sigma_{xy} &= \sigma_{xz} = 0\,,\\
\sigma_{yz} &= \tfrac{1}{2}(c_{11} - c_{12})\,\gamma\,,
\end{aligned} \tag{32}$$

Conflicts of interest

There are no conflicts to declare.

Acknowledgements

We thank R. Höhler and T. Baumberger for fruitful discussions. We acknowledge financial support from Centre national d'Etudes Spatiales (research agreement CNES/CNRS number 180113), and the European Space Agency (Soft Matter Dynamics MAP grant AO 09-943).

Notes and references

1 I. Cantat, S. Cohen-Addad, F. Elias, F. Graner, R. Höhler, O. Pitois, F. Rouyer and A. Saint-Jalmes, *Foams: Structure and*

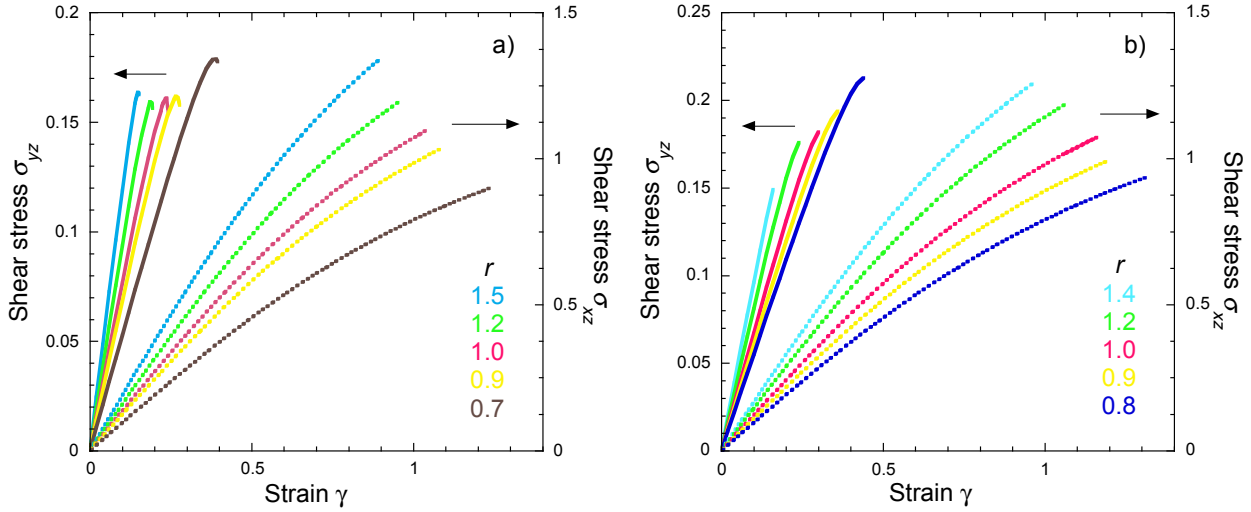

Fig. 13 Stress-strain curves simulated for y-z shear (left axis) and x-z shear (right axis): a) bilayers and, b) trilayers, for different confinement ratios r as labeled. The stress is expressed in $T/V^{1/3}$ units.

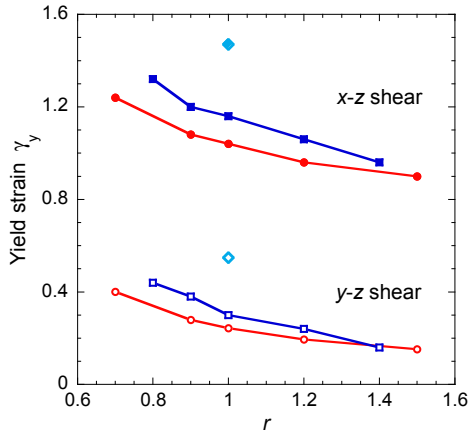

Fig. 14 Yield strain γ_y as a function of the confinement ratio r for a bilayer (●, ○), a trilayer (■, □) and a Kelvin foam (⧫, ◊). Filled symbols correspond to x-z shear, and empty symbols to y-z shear. Lines are guides to the eyes.

Dynamics, Oxford University Press, Oxford, 2013.

2 D. Weaire and S. Hutzler, *The Physics of Foams*, Oxford University Press, 1999.

3 P. Stevenson, *Foam Engineering: Fundamentals and Applications*, J. Wiley, 2012.

4 R. Farajzadeh, A. Andrianov, R. Krastev, G. J. Hirasaki and W. R. Rossen, *Advances in Colloid and Interface Science*, 2012, **183-184**, 1–13.

5 L. Zhong, J. Szecsody, M. Oostrom, M. Truex, X. Shen and X. Li, *Journal of Hazardous Materials*, 2011, **191**, 249–257.

6 K. Ma, R. Liontas, C. A. Conn, G. J. Hirasaki and S. L. Biswal, *Soft Matter*, 2012, **8**, 10669–10675.

7 B. Geraud, S. A. Jones, I. Cantat, B. Dollet and Y. Meheust, *Water Resources Research*, 2016, **52**, 773–790.

8 S. A. Jones, N. Getrouw and S. Vincent-Bonnieu, *Soft Matter*, 2018, **14**, 3490–3496.

9 M. J. Shojaei, A. Rodriguez de Castro, Y. Meheust and N. Shokri, *Journal of Colloid and Interface Science*, 2019, **552**, 464–475.

10 W. Drenckhan, S. J. Cox, G. Delaney, H. Holste, D. Weaire and N. Kern, *Colloids and Surfaces A*, 2005, **263**, 52–64.

11 P. Marmottant and J.-P. Raven, *Soft Matter*, 2009, **5**, 3385–3388.

12 N. Bremond and J. Bibette, *Soft Matter*, 2012, **8**, 10549–10559.

13 M. Lee, J. W. Collins, D. M. Aubrecht, R. A. Sperling, L. Solomon, J.-W. Ha, G.-R. Yi, D. A. Weitz and V. N. Manoharan, *Lab on a Chip*, 2014, **14**, 509–513.

14 A. Huerre, V. Miralles and M.-C. Jullien, *Soft Matter*, 2014, **10**, 6888–6902.

15 S. Cohen-Addad and R. Höhler, *Current Opinion in Colloid and Interface Science*, 2014, **19**, 536–548.

16 B. Dollet and C. Raufaste, *Comptes Rendus Physique*, 2014, **15**, 731–747.

17 S. J. Cox, S. Neethling, W. R. Rossen, W. Schleifenbaum, P. Schmidt-Wellenburg and J. J. Cilliers, *Colloids and Surfaces A: Physicochemical and Engineering Aspects*, 2004, **245**, 143–151.

18 R. Höhler, Y. Yip Cheung Sang, E. Lorenceau and S. Cohen-Addad, *Langmuir*, 2008, **24**, 418–425.

19 W. Drenckhan and D. Langevin, *Current Opinion in Colloid and Interface Science*, 2010, **15**, 341–358.

20 A. Testouri, L. R. Arriaga, C. Honorez, M. Ranft, J. Rodrigues, A. van der Net, A. Lecchi, A. Salonen, E. Rio, R. M. Guillermic, D. Langevin and W. Drenckhan, *Colloids and Surfaces A: Physicochemical and Engineering Aspects*, 2012, **413**, 17–24.

21 L. Fejes-Toth, *Bull. Amer. Math. Soc.*, 1964, **70**, 468–481.

22 A. M. Kraynik and D. A. Reinelt, *Journal of Colloid and Interface Science*, 1996, **181**, 511–520.

23 K. Brakke, *The Surface Evolver is freely available at http://www.susqu.edu/facstaff/b/brakke/evolver/*.

24 G. Batchelor, *J. Fluid. Mech.*, 1970, **41**, 545–570.
25 A. M. Kraynik, D. A. Reinelt and F. van Swol, *Physical Review E*, 2003, **67**, 031403–11.
26 V. Labiausse, R. Hohler and S. Cohen-Addad, *Journal of Rheology*, 2007, **51**, 479–492.
27 D. A. Reinelt, *Journal of Rheology*, 1993, **37**, 1117–1139.
28 D. A. Reinelt and A. M. Kraynik, *Journal of Fluid Mechanics*, 1996, **311**, 327–343.
29 H. M. Princen, *Journal of Colloid and Interface Science*, 1983, **91**, 160–175.
30 J. Nye, *Physical properties of crystals*, Clarendon Press, Oxford, 1985.